IEEE Access
Multidisciplinary | Rapid Review | Open Access Journal

Received 5 April 2024, accepted 9 May 2024, date of publication 15 May 2024, date of current version 23 May 2024.

Digital Object Identifier 10.1109/ACCESS.2024.3401410

RESEARCH ARTICLE

A Modular Approach for the Design of Quadruple Ridged Flared Horn Antenna Feeds

ÓSCAR GARCÍA-PÉREZ[1], FÉLIX TERCERO[1], ALEJANDRO BALDOMINOS[2], GABRIEL GÓMEZ-MOLINA[1], ALBERTO GARCÍA-MERINO[1], DAVID REGAJO-RODRÍGUEZ[1], AND ROCÍO SÁNCHEZ-MONTERO[3], (Member, IEEE)

[1]Yebes Observatory, Instituto Geográfico Nacional, Yebes, 19141 Guadalajara, Spain
[2]Digital Payload Team, Airbus Defence and Space, SG1 2AS Stevenage, U.K.
[3]Signal Theory and Communications Department, University of Alcalá, Alcalá de Henares, 28801 Madrid, Spain

Corresponding author: Óscar García-Pérez (ogarcia@oan.es)

ABSTRACT This paper presents the methodology followed for the design of a quad-ridged flared horn (QRFH) feed for the VLBI Global Observing System (VGOS) antennas. The study demonstrates the potential undesired effects caused by the presence of non-fundamental modes at the throat of the horn antenna, and how they can be avoided following some design considerations. The approach consists of a separate design of the feeding transition and the flared section of the horn, and it can be extrapolated to other implementations. Firstly, the geometry of the coaxial to quad-ridged waveguide (QRWG) transition is defined. The proposed design technique ensures negligible propagation of higher order modes at the waveguide interface. Secondly, the ridges and sidewall profiles of the flared part are optimized to achieve the desired performance in terms of input reflection and aperture efficiency on the VGOS 13.2-meter displaced-axis two-reflector radio telescope. Following the optimized design, five QRFH antenna units have been manufactured and tested, all showing reflection coefficients better than -10 dB and predicted aperture efficiencies better than 55 % in the band from 2.2 to 14 GHz. The excellent agreement between simulations and experimental results demonstrates the validity of the proposed methodology.

INDEX TERMS Antenna feeds, horn antennas, quadruple-ridged flared horn (QRFH), radio astronomy, ultra wideband antennas.

I. INTRODUCTION

Modern radio telescopes tend to use receivers with ever increasing bandwidths. Traditional radio astronomy front ends, based primarily on corrugated horn feeds and waveguide orthomode transducers, are typically limited to bandwidths of about one octave [1]. However, nowadays there are different examples of systems that already consider multi-octave receivers, such as the VLBI Global Observing System (VGOS) [2] or some bands of the Square Kilometre Array (SKA) [3]. Consequently, during the last years multiple new antenna topologies have been proposed as wideband radio telescope feeds for such projects [4], [5], [6], [7], [8], [9]. Among the wideband feed types cited before, the quadruple-ridged flared horn (QRFH) antenna [9] offers the most straightforward approach to provide two orthogonal single-ended 50-Ω outputs to which directly attach the low noise amplifiers (LNA), instead of requiring differential-mode excitations. This is accomplished by integrating two wideband coaxial air lines, and therefore avoiding the losses of external passive baluns or the complexity of differential-like LNAs. In addition, its all-metal structure makes it a low-loss, easy-to-cool and robust antenna, and therefore very adequate for cryogenic receivers. In this context, during the last decade multiple QRFH designs for radio astronomy applications have been proposed, with relative bandwidths up to 10:1 and maximum frequencies of operation as high as 50 GHz [9], [10], [11], [12], [13], [14], [15], [16], [17].

The performance of the QRFH as a feed heavily relies on the conversions between waveguide modes along the horn, and ultimately on the modal distribution at the aperture at the different frequencies [9]. Nevertheless, the excitation

The associate editor coordinating the review of this manuscript and approving it for publication was Chinmoy Saha.

of spurious higher order modes in the zone of the coaxial to quad-ridged waveguide (QRWG) transition can seriously deteriorate the radiation pattern at some specific frequencies [11], [18]. These effects are sometimes narrowband, and difficult to detect during the design phase, especially when the transition and the flared parts are blindly optimized together as a whole. The worst-case scenario is the appearance of the so-called trapped modes [19]. However, just the mere presence of non-fundamental modes at the throat of the QRFH –not necessarily trapped– may result into a degraded illumination on the reflector [17]. It must also be noticed that the trapped modes in QRFH transitions can be analytically predicted [20], but obtaining the whole modal distribution at the QRWG interface requires a full-wave simulation.

To solve the aforementioned problem, in [11] they propose a separate design of the feeding structure based on a quadraxial network to attenuate the higher order modes at the throat of the QRFH. However, apart from its complexity, this implementation presents the drawbacks previously mentioned for differentially fed antennas. Furthermore, the effectiveness of the solution relies on having well balanced differential excitations, which can be hard to achieve with real baluns in wide bands. In [13] they also propose a QRFH design with stand-alone optimizations of the transition and the flared parts. The transition uses the traditional single-ended configuration, but the excitation of higher order modes is not addressed. As a result, a final reoptimization of the whole feed was needed, since they found the transition had unexpected effects on the radiation performance. Up to this point, to the best of the author's knowledge, a study on the excitation of higher order modes –and techniques to mitigate them– in single-ended transitions for QRFH antennas has not been treated in the literature.

This paper presents the development of a QRFH feed with 6.4:1 bandwidth for geodetic radio telescopes. The proposed methodology involves designing the coaxial-to-QRWG transition and the flared part separately, as depicted in Figure 1 (a). The modal interactions in the single-ended transition are thoroughly analyzed, and the potential detrimental effects on the radiation pattern are demonstrated. It is shown that, following a few design guidelines, it is possible to mitigate the undesired higher order modes at the QRWG interface at negligible levels, while maintaining good impedance matching at the two coaxial ports. In addition, the separate design of the transition helps simplify the subsequent optimization of the flared part, since it reduces the simulation domain and the parameters, and enables the assumption of pure fundamental mode excitation at the QRWG port. The experimental results obtained from five identical QRFH feeds validate the presented theoretical principles.

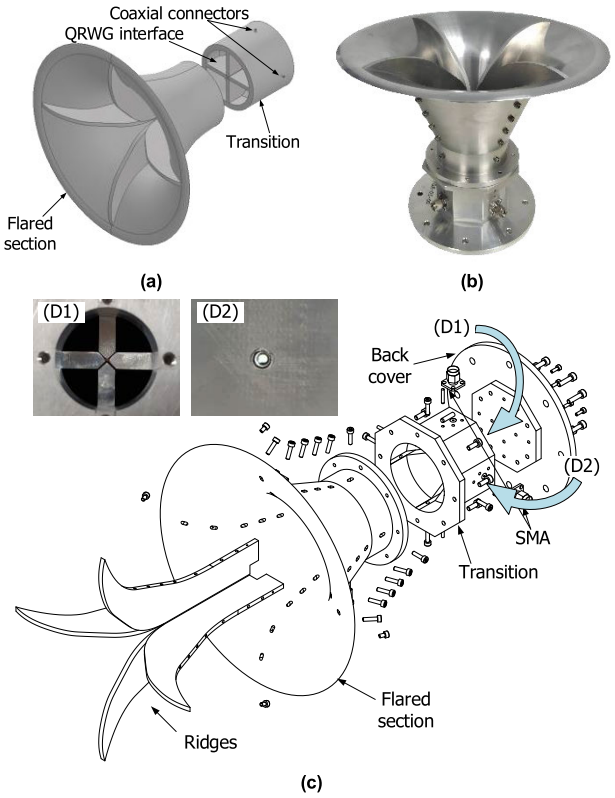

FIGURE 1. (a)Proposed QRFH topology. (b) Manufactured QRFH feed. (c) Assembly of the QRFH antenna, and details of the alignment of the ridges seen from the cavity (D1) and alignment of the holes for the air-dielectric coaxial line (D2).

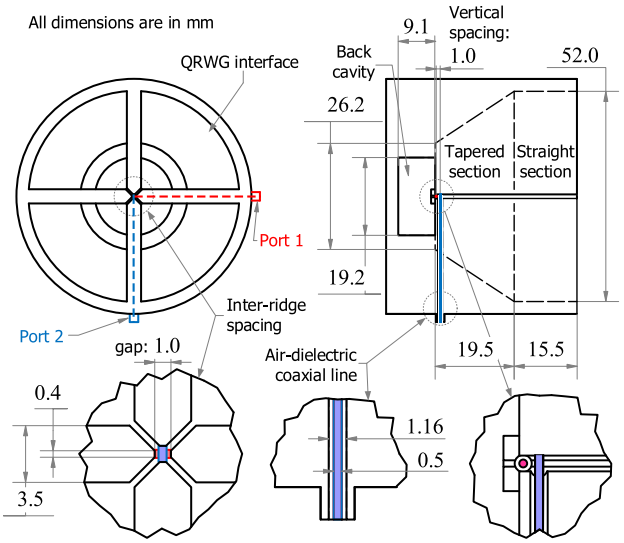

FIGURE 2. Scheme of the optimized coaxial-to-QRWG transition.

II. DESIGN AND OPTIMIZATION

A. COAXIAL TO QRWG TRANSITION

The proposed design for the feeding structure of the QRFH is depicted in Figure 2, which transitions between two orthogonal SMA-type coaxial connectors (ports 1 and 2) and the QRWG interface. To provide the desired dual-linear polarization, two orthogonal air-dielectric coaxial lines are used as baluns. These lines are very close to one end of the QRWG and are spaced 1 mm apart to prevent contact. The dimensions of the outer circular waveguide and the ridges

have been defined based on various design constraints, such as the width and impedance of the coaxial lines, the cutoff frequency of the fundamental mode, and the manufacturing precision and tolerances. In a QRWG, the effect of loading a circular waveguide with the four ridges allows increasing the achievable bandwidth if the second-lowest mode is effectively suppressed or not excited. In addition, the waveguide impedance is proportional to the ridge gap, so reducing the gap allows decreasing the wave impedance of the circular waveguide from some hundreds of ohms to levels comparable to the characteristic impedance of a transmission line. Consequently, a heavily loaded waveguide (i.e., very narrow ridge gap) is required in this case to achieve both wideband response and good matching to the relatively low impedance of the coaxial lines (50 Ω) [21].

The proposed transition consists of three parts along its structure: a cylindrical back cavity, a tapered QRWG section and a straight QRWG section. Despite its simplicity, it has been found that this topology is versatile enough to provide control over the propagation of modes at the QRWG interface. The cutoff frequencies of the propagating modes along the QRWG transition within the band of interest are represented in Figure 3 (we have followed the modal notation used in [21]). It must be noticed that the cutoff frequencies of all the modes are by design monotonically decreasing from the feeding point to the QRWG interface, and they continue along the whole feed to the aperture as the sidewalls and ridges progressively widen. This ensures the absence of local minima (the so-called wells in [19]) and therefore avoids the possibility of having trapped modes.

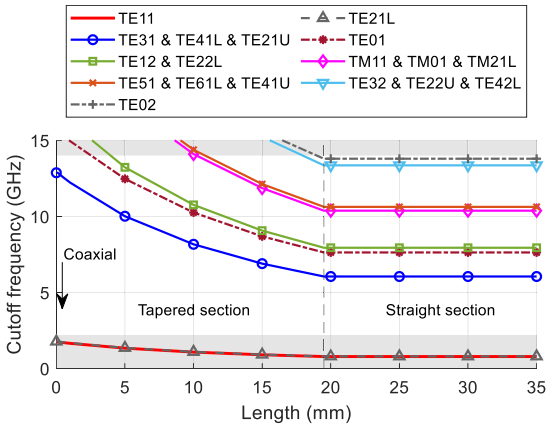

FIGURE 3. Cutoff frequencies of the different modes along the transition, from the coaxial line (left) to the QRWG interface (right).

It is widely known that a differential excitation between two opposite ridges in a QRWG efficiently couples to the fundamental TE_{11} mode. However, this does not prevent other higher modes from appearing above their respective cutoff frequencies. In particular, given the four-fold symmetry of the QRWG, other odd-order TE and TM modes are also likely to be excited [9]. Among the modes in Figure 3, these correspond to TE_{31}, TE_{12}, TM_{11}, TE_{51} and TE_{32}. As it can be observed in Figure 4, such modes present both electric-type symmetry (i.e., E_t=0) at the plane containing the excitation vector and magnetic-type symmetry (i.e., H_t=0) at the orthogonal plane. Apart from these, it is also worth mentioning the TE_{21L} mode which, in heavily loaded QRWGs, has a cutoff frequency very close to the fundamental mode and plays a role when using a single-ended excitation that breaks the symmetry in the orthogonal plane.

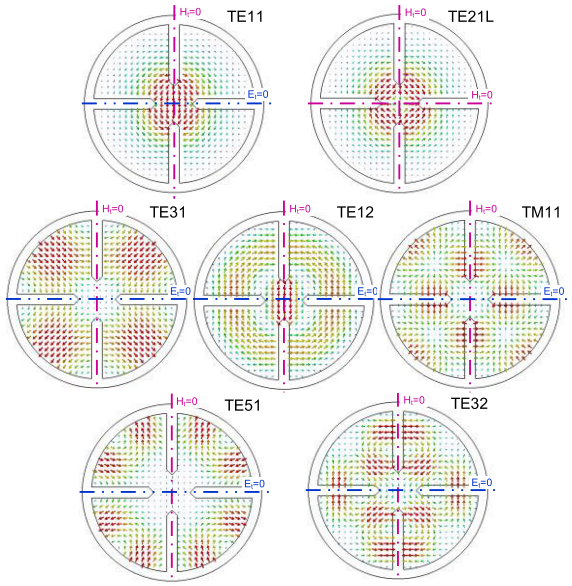

FIGURE 4. E-field distributions of some of the main modes in a generic QRWG (the gap is wider than in the present design for better visualization of the fields). The dash-dotted lines indicate the type of symmetry: electric (E_t=0) or magnetic (H_t=0), where E_t and H_t denote the tangential electric and magnetic fields respectively.

In order to illustrate the effect of the different parts of the transition on the propagation of the different modes, a series of simulations performed in CST [22] are shown in Figure 5. The first topology consists of a straight QRWG fed by an ideal 50-Ω discrete port from one end, and a relatively wide back cavity. In this configuration, as it can be observed in Figure 5 (a), although the impedance matching is relatively good across the bandwidth, a variety of modes are propagated as the frequency increases. Such modes induce undesired effects on the radiation pattern of the feed, as it will be demonstrated later with the efficiency results.

The effect of narrowing the back cavity is shown in Figure 5 (b). Although the cavity is typically used just for impedance matching purposes, this simulation shows that it can play a fundamental role in filtering out many of the unwanted higher order modes. Specifically, those modes with most of their energy distributed in the four outer troughs of the waveguide (i.e., TE_{31}, TM_{11}, TE_{51} and TE_{32}) are significantly attenuated. This indicates that such modes are somehow coupled through the cavity, under the edges of the ridges, and therefore cancelled out when the cavity is narrow enough to cut off its propagation. On the other hand, the modes with most of their energy concentrated in the center

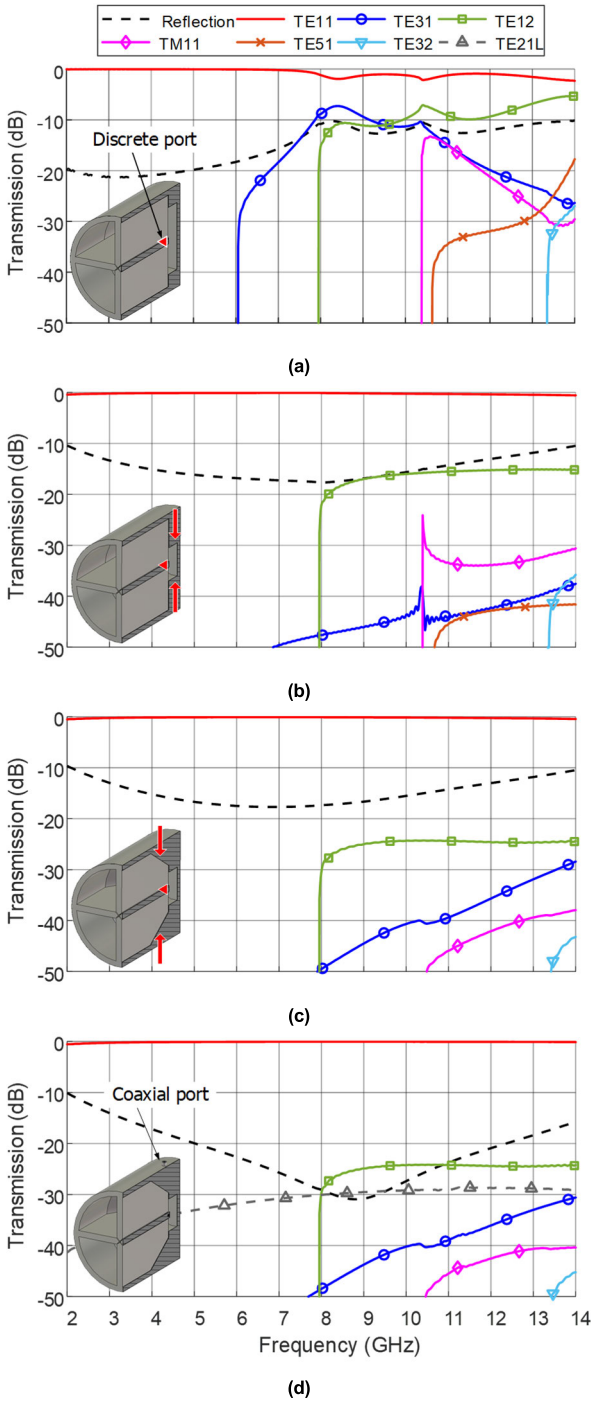

FIGURE 5. Simulated transmission between the single-ended excitation and the different modes at the QRWG for cumulative modifications in the transition structure: (a) wide back cavity QRWG and discrete port, (b) effect of narrowing the back cavity, (c) effect of tapering the sidewall at the zone of the excitation, (d) final configuration with a coaxial connector.

gap area (i.e., TE_{11} and TE_{12}) are much less affected, except for the variation in the overall power distribution. The previous reasoning seems to be confirmed by the results shown in Figure 6, with snapshots of the simulated electric field magnitude for the different variations of the transition. The first column shows a significant concentration of energy in the

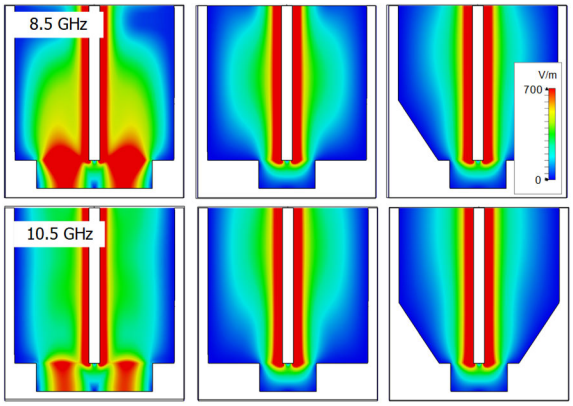

FIGURE 6. Section view with simulated E-fields along the transition for different variations of the geometry (from left to right), at 8.5 GHz (up) and 10.5 GHz (down). It represents the maximum magnitude (all the same scale) in a plane parallel to the excitation vector, separated 3 mm apart from the center axis.

cavity at 8.5 and 10.5 GHz in the scenario of Figure 5 (a), which practically disappears in the following scenario when narrowing its diameter.

The next step, shown in Figure 5 (c), consists of tapering the sidewall of the QRWG. As it was shown in Figure 3, this increases the cutoff frequencies of all the modes in the zone of the feeding point, although the effect is more pronounced for the higher order modes. The most noticeable effect in this case is a reduction of about 10 dB for the TE_{12} mode.

Finally, the impact of substituting the ideal differential ports with coaxial lines is shown in Figure 5 (d). The asymmetry introduced by the single-ended coaxial line enables the propagation of modes with different types of electric-magnetic symmetries. In this case the TE_{21L} mode is the only one that appears with a significant level in the plot. In this regard, it is worth mentioning that the diameter of the coaxial line does have an effect. Using a thinner line induces less asymmetry and is therefore less prone to excite such even-order modes. Nevertheless, in this final configuration the higher order modes are all constrained below -24 dB. It must be noted that this level is in the order of –even better than– that obtained with more complex topologies in comparable frequency ranges, such as the quadraxial feeding network proposed in [11]. In practice, it has been observed that non-fundamental modes below -20 dB already provide quite similar performance compared to pure TE_{11}-mode excitation when connecting the transition to the flared section. In addition, the reflection coefficient is below -10 dB in the whole band of interest.

B. FLARED SECTION

Figure 7 illustrates the flared section of the QRFH, which is composed of a ridge profile that defines the internal shape of the ridge, and a sidewall profile that determines the horn's cylindrical symmetry. In addition, the aperture edges have been finished with a curved surface to improve the

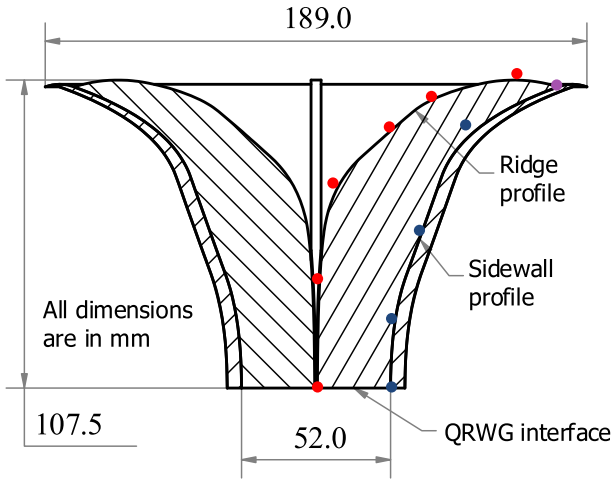

FIGURE 7. Scheme of the optimized flared section of the QRFH. The red and blue dots represent the control points of the splines used for the ridge and sidewall profiles respectively (note that the final points of both profiles are forced to be coincident).

matching conditions between the horn modes and the free space radiation [23].

This study employs third-order standard B-splines for the ridges and sidewall profiles of the QRFH. In mathematical modelling, a third-order B-spline is a piecewise parametric curve expressed by a collection of control points and second-degree basis functions [24]. In this case, the splines are two-dimensional, so each control point is defined by an x-y coordinate pair. The B-spline curve $\boldsymbol{C}(u)$can be defined as

$$\boldsymbol{C}(u) = \sum_{i=0}^{n} N_{i,2}(u)\boldsymbol{P_i} \tag{1}$$

where $u \in [0, 1]$ is the parametric variable, $N_{i,2}(u)$ denote the basis functions, and $\boldsymbol{P_i}$ is the set of $n+1$ control points. The second-degree basis functions $N_{i,2}(u)$ can be constructed by means of the so-called Cox-de Boor recursive formula as

$$\begin{aligned} N_{i,0}(u) &= \begin{cases} 1 & \text{if } u_i \le u < u_{i+1} \\ 0 & \text{otherwise} \end{cases} \\ &\cdots \\ N_{i,p}(u) &= \frac{u - u_i}{u_{i+p} - u_i} N_{i,p-1}(u) \\ &\quad + \frac{u_{i+p+1} - u}{u_{i+p+1} - u_{i+1}} N_{i+1,p-1}(u) \end{aligned} \tag{2}$$

where p denotes the degree of the polynomial ($p = 2$ for third-order B-splines), and u_i are the so-called knot points. The series of $m+1$ knots $U = \{0, \ldots, u_i, \ldots, 1\}$ determine the breakpoints between the pieces of adjacent polynomials, and form a nondecreasing sequence of real numbers in the interval [0, 1]. The relationship between the number of knots, the order of the polynomials and the number of control points is given by

$$m = p + n + 1. \tag{3}$$

In this case, the knot points are distributed uniformly, and set to have the curve starting in the first control point ($\boldsymbol{P}_0$) and ending in the last control point ($\boldsymbol{P}_n$) [24].

In practice, each B-spline is simply defined by a series of control points. In this case, seven and five control points have been used to define the ridge and the sidewall profiles respectively (see the dots in Figure 7). Third-order B-splines present some inherent advantages compared to simple exponential profiles: they can represent a richer variety of smooth curves; and they allow local control, which means that modifying a single control point only affects a limited range of the curve due to the piecewise nature. As a counterpart, they require more parameters to optimize.

Since the dimensions of the QRWG interface are preestablished from the previous design of the transition, and the last control point near to the aperture is common to both profiles, this gives a total of 16 parameters to be optimized. This number is comparable to that required to optimize a whole QRFH with a simpler exponential profile [9], [15], and is much lower than the parameters needed in other QRFH designs based on splines [13] or discrete points [16]. Therefore, the present approach provides a reasonable tradeoff between versatility and complexity, taking advantage of the flexibility given by the spline-defined geometries but with a restricted number of variables for an efficient performance of the optimization algorithm. The flared section was optimized using a genetic algorithm built in Matlab [25]. Custom functions were developed to generate a geometrically feasible population, which was evaluated using a multi-objective cost function. The cost functions were designed to minimize the input reflection at the QRWG interface, with a target below -10 dB, and to maximize the aperture efficiency, with a target above 50 %. The cost functions were evaluated in CST from electromagnetic simulations of each individual in the population. The resulting cost functions were then sorted by the genetic algorithm back in Matlab.

The optimization results are presented in Figure 8, which shows that both goals were achieved over almost the entire frequency band of interest. The optimized geometry features an aperture diameter of 189 mm and a flared section length of 107.5 mm. The results demonstrate that the chosen approach is effective in achieving the desired optimization goals, and therefore fulfilling the specifications for VGOS.

Apart from the final optimization results, Figure 8 also includes a parametric analysis varying the width and the length of the horn. This study serves to evaluate the result of the optimization, to see the robustness of the design and to identify the critical parts of the geometry. According to the results in Figure 8 (a)-(b), when the antenna is scaled in width the design is relatively stable in terms of both impedance matching and efficiency for a wide range of values. Nevertheless, a progressive degradation in efficiency is observed at higher frequencies for wider apertures, due to poorer illumination efficiency. On the other hand, scaling the antenna in length has a more noticeable effect, as it can be seen in Figure 8 (c)-(d). A longer flared

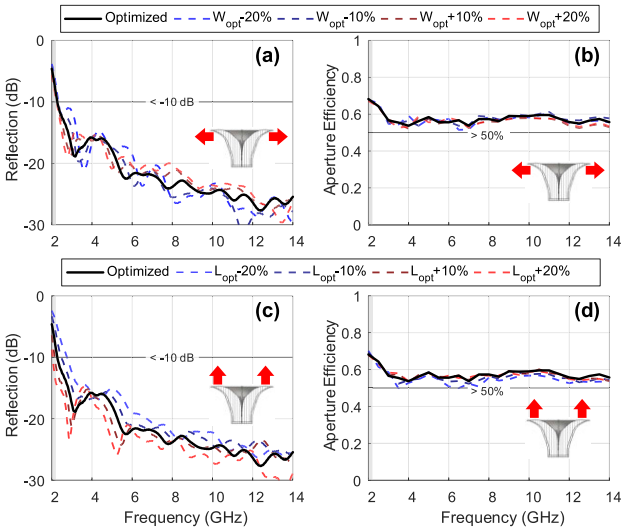

FIGURE 8. Simulated results of the optimized flared section of the QRFH: reflection coefficient at the QRWG interface (left) and estimated aperture efficiency (right). The plots also show a parametric study based on the optimized geometry, scaling up/down the width (a)(b) and the length (c)(d) of the antenna respectively.

section greatly improves the reflection coefficient in the lower part of the band. However, the efficiency appears to worsen both when lengthening or shortening the structure. Therefore, the final geometry seems to be well optimized for the chosen optimization goals and the corresponding band of interest, and it possesses an adequate length-width ratio.

III. ASSEMBLY AND MEASUREMENTS

A. MANUFACTURING

The manufacturing and assembly process of the QRFH antennas is crucial, especially for achieving good reflection coefficients. Previous works have reported difficulties to obtain good agreement between measurements and simulations, and consequently to get measured return losses better than −10 dB in bandwidths larger than 5:1 [9], [10], [11], [12], [13], [14], [15], [16], [17].

In this case, a first set of five QRFH antennas were manufactured following the optimized design presented in Section II. The antennas are entirely made of aluminum (except the coaxial connectors), have overall dimensions of 162 mm in length and 189 mm in width, and a weight of approximately 1 kg (see Figure 1 (b)). The assembly drawings are depicted in Figure 1 (c). The outer part of the horn is divided into three separate pieces, namely the transition and the flared sections, and a back cover that also serves to attach the antenna to the cryostat. Inside the horn, each one of the four ridges is made in a single piece and is assembled passing through both the transition and the flared sections.

Two of the most delicate parts of the assembly process are illustrated in the insets of Figure 1 (c). The first picture (D1) shows the alignment of the four ridges as seen from the open back cavity. Achieving perpendicularity and the desired narrow gap dimensions between the ridges is critical for the antenna operation. According to the simulations, the gaps should be within a range of 1±0.1 mm to ensure the desired impedance matching. The actual gaps in the five manufactured antennas, measured with an ultra-high precision metrology system, are all within a range of 1±0.03 mm. The second picture (D2) shows the alignment of the holes for the coaxial line. In the setup, there is a part where the center conductor passes through a hole in one of the ridges to form the air-dielectric coaxial line. On the opposite ridge, beyond the gap, there is a hole machined to fit the size of the inner conductor, locking the wire in place, and effectively short-circuiting the line by friction. During manufacturing, it is essential to ensure that the drill holes in each pair of ridges are concentric to avoid undesired effects in the transmission line. The maximum tolerable concentricity deviation has been estimated as 0.1 mm in radius, whereas the actual deviation measured on the five antenna units is below 0.09 mm. These results demonstrate the high precision achieved during the manufacturing and assembly process.

B. EXPERIMENTAL RESULTS

The following results compare the simulations, obtained from the stand-alone flared section (QRWG port) and the whole QRFH feed (coaxial port), with the measurements obtained from the manufactured antennas. The linear-polarization beam patterns have been measured using a spherical near-field range in an anechoic chamber. Each port has been measured independently –using a matched load for the unused port– although, in practice, the obtained results are fundamentally the same for both ports due to the negligible separation between them and the symmetries of the antenna. Therefore, without loss of generality, the results presented in this Section with coaxial feeding correspond to port 1, unless the connector number is explicitly indicated. The aim of this comparison is to validate both the design methodology and the manufacturing and assembly process. Some of the main figures of merit of the QRFH design are summarized in Table 1. Apart from the simulated and measured results, the table also includes the variability in such parameters obtained from the five manufactured antennas. The low discrepancies between the units serve to remark the robustness of the mechanical design and the repeatability of the manufacturing and assembly of the antenna components.

The simulated and measured radiation patterns of the QRFH antenna at 2.5, 8 and 14 GHz are presented in Figure 9. From the simulated results, there is no noticeable difference between simulating the flared section with a pure TE_{11} excitation or attaching the optimized coaxial-to-QRWG transition, indicating that the higher order modes are effectively suppressed in the transition. This result is also well reproduced by the measurements.

The simulated and measured beamwidth and the maximum cross-polarization level of the QRFH antenna are shown in Figure 10. Again, consistent agreement is achieved between the waveguide-port simulation, the coaxial-port simulation,

TABLE 1. Summary of results of the implemented QRFH feeds (2.2-14.0 GHz).

Parameter	Simulation (coaxial port)	Measurement (avg.)	Variability (meas. 5 units)
10dB-BW (E-plane)	110 – 146 º	109 – 144 º	1.4 º (*)
10dB-BW (H-plane)	56 – 128 º	50 – 124 º	1.2 º (*)
Max. cross-polar	-16.7 – -5.4 dB	-15.8 – -5.2 dB	0.26 dB (*)
Phase center	-44.6 – -26.3 mm	-41.7 – -20.5 mm	0.34 mm (*)
Efficiency	0.54 – 0.63	0.55 – 0.67	0.005 (*)
Max. s_{11}	-10.0 dB	-10.6 dB	0.7 dB (**)
Max. s_{22}	-10.9 dB	-11.0 dB	1.1 dB (**)
Max. s_{21}	-	-33.9 dB	4.4 dB (**)

*: Average of standard deviations at each frequency across the bandwidth.
**: Standard deviation.

and the experimental results. As it is usual in this type of horn antennas, the beamwidth remains relatively constant with frequency for the E-plane cut, whereas it progressively narrows at higher frequencies for the H-plane cut [9]. With respect to the normalized cross-polarization level, it typically remains below −8 dB in the band of interest, with a maximum peak of about −5 dB at 3.5 GHz.

The phase center position computed from the simulated and measured radiation patterns is represented in Figure 11. For the measured patterns, the phase center varies between 24 and 42 mm from the aperture in the band of interest. Nevertheless, the greater variation occurs at lower frequencies, where the radio telescope is more tolerant to defocus, and remains quite constant at higher frequencies above 6 GHz. The optimal location of the reflector focal point relative to the feed was determined to be at 39 mm from the aperture inside the horn, as the position that maximizes the average aperture efficiency. The maximum relative axial defocus of the feed is 0.22λ and occurs at 4.5 GHz.

The measured radiation patterns between 2 and 14 GHz, with steps of 500 MHz, are displayed in Figure 12. The VGOS radio telescope is a displaced-axis two-reflector antenna [26], also known sometimes as ring-focus, with a half-subtended angle of 65 deg. For such system, the optimal gaussian beam has a taper of 13.5 dB, which has been depicted with the copolar plots as a reference. The obtained copolar patterns are consistent with what is expected from a QRFH feed, with a nearly constant beamwidth in E-plane, and the beam narrowing with frequency in H-plane. In the case of the normalized cross-polar pattern, the levels are in line with what is usually obtained in other wideband feeds of similar specifications presented in the literature (e.g., [11]). It is worth mentioning that there are QRFH designs that offer more constant beam shape across the band and improved cross-polarization levels by introducing a multi-dielectric insert [14], although such

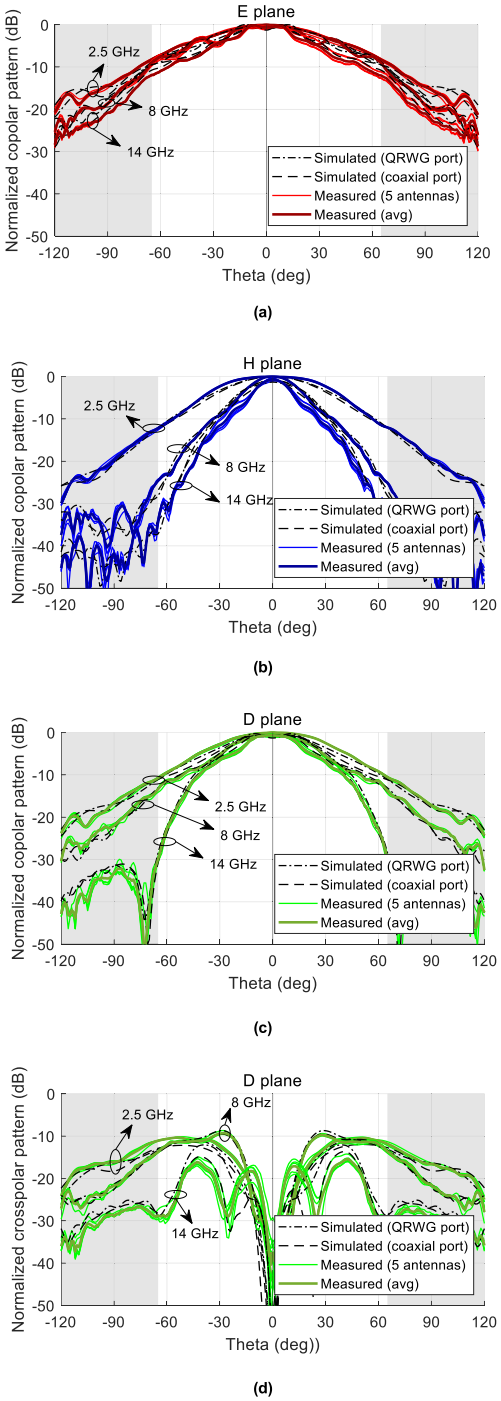

FIGURE 9. Simulated and measured radiation patterns of the QRFH antenna at 2.5, 8 and 14 GHz: (a) E-plane copolar, (b) H-plane copolar, (c) D-plane copolar, and (d) D-plane cross-polar.

configuration was discarded in the present design due to its complexity.

The computed aperture efficiency on the 13.2-m VGOS radio telescope, obtained from the simulated and measured radiation patterns of the QRFH feed, is represented in Figure 13. Once again, the results demonstrate a high degree of agreement. Despite the well-known lack of rotational symmetry of the QRFH feed pattern, the aperture

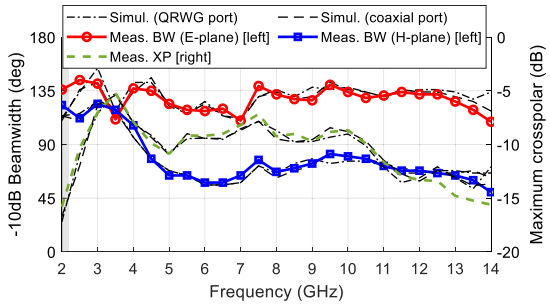

FIGURE 10. Simulated and measured 10dB-beamwidth (left) and maximum cross-polarization level (right) of the QRFH antenna.

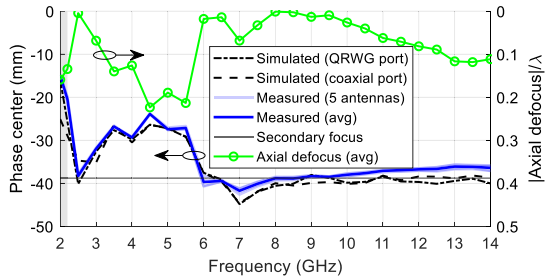

FIGURE 11. Phase center from the measured and simulated radiation patterns of the QRFH antenna (distance from aperture, inside the horn), and axial defocus in terms of wavelength.

efficiency is better than 55 % across an entire 6.4:1 bandwidth. All these efficiency results have been analytically computed with Matlab and confirmed with GRASP [27]. In addition, the contributions of the different sub-efficiencies are also represented [28], being the illumination efficiency the main detractor for the total efficiency.

In order to illustrate the impact of the unwanted non-fundamental modes at the throat of the horn, the simulated efficiency obtained with the transition design of Figure 5 (a) has also been included in the results of Figure 13. In such a case, even though the input matching of the QRFH is comparable to the case of the optimized transition, the efficiency dramatically decays at the frequencies at which the contribution of the higher order modes is more significant, due to distortions in the radiation pattern. Intermediate cases, between the geometry of Figure 5 (a) and the optimized transition, may lead to more subtle effects that can still seriously degrade the efficiency at specific frequencies. These effects can easily go unnoticed in case of blindly optimizing the feed as a whole without addressing the propagation of higher order modes at the transition.

With respect to the telescope sensitivity at zenith, the average computed system equivalent flux density (SEFD) is about 1200 Jy, with a maximum of 1500 Jy. The SEFD is a figure of merit commonly used in radio astronomy defined as the flux density of a radio source that doubles the system temperature, so that a lower value of SEFD indicates better sensitivity [29]. For the calculation, it has been assumed that the overall receiver noise temperature is 30 K, the atmosphere contribution at these frequencies is between 5 and 9 K, and the ground temperature is 300 K. This preliminary estimation

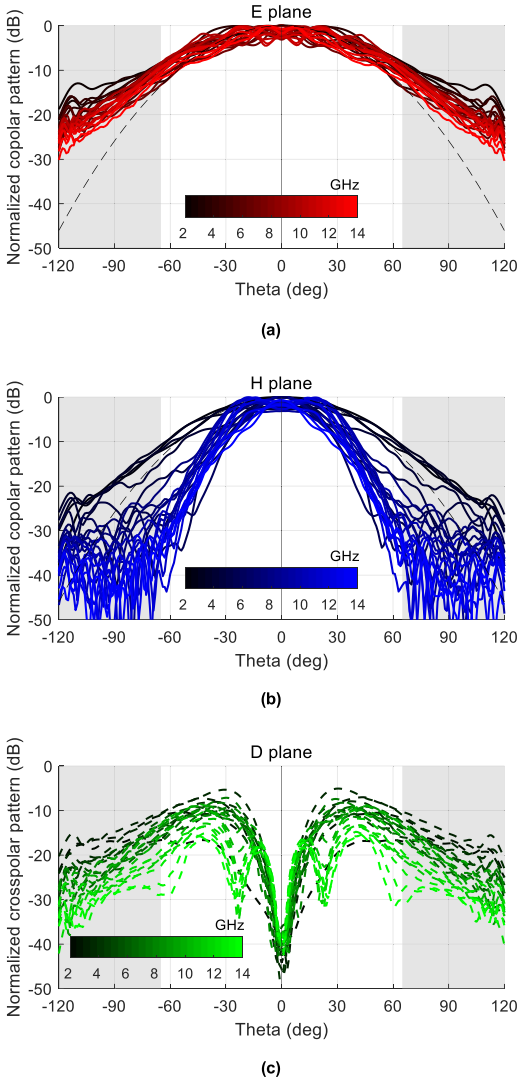

FIGURE 12. Measured radiation patterns of the five QRFH antennas (average): (a) E-plane copolar, (b) H-plane copolar, and (c) D-plane cross-polar. The dashed line in (a) and (b) represents the optimal gaussian pattern for the ring-focus reflector as a reference.

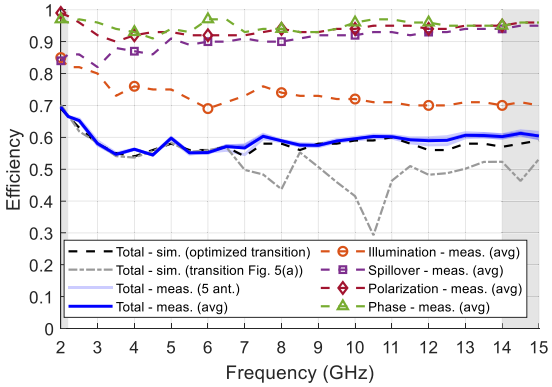

FIGURE 13. Computed aperture efficiency (total) and sub-efficiencies on the VGOS radio telescope from the simulated and measured radiation patterns of the QRFH antenna.

meets the VGOS specification of 2500 Jy [30] by a wide margin. In any case, the final performance will depend on

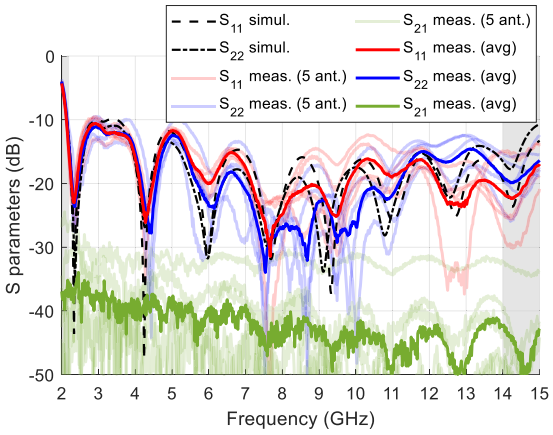

FIGURE 14. Simulated and measured S-parameters of the QRFH antenna.

a variety of factors, such as the particular implementation of the receiver, the site conditions or the elevation angles.

Finally, the simulated and measured S-parameters are shown in Figure 14. In this case there is more variability among the different antenna units. This is attributed to the assembly of the center conductor of the coaxial lines, which has been observed to be a critical process. In any case, the obtained reflection coefficients (s_{11}, s_{22}) are below −10 dB and the isolation between ports (s_{21}) is better than −30 dB for the five manufactured QRFH antennas across the band of interest.

A comparative view of the present design with respect to other QRFH antennas proposed as feeds for radio astronomy applications in comparable frequency ranges is presented in Table 2. It must be noticed that the main contributions claimed in this paper are more related to the modal analysis and the proposed design methodology, and not so much to severely improving the performance of other state-of-the-art designs. Nonetheless, the presented solution comparatively achieves great performance in terms of low reflection and high aperture efficiency over a bandwidth exceeding 6:1. One of the aspects to highlight is that, although many of the designs presented in the literature predict reflection coefficients in simulation better than −10 dB, the measured response of the prototype commonly surpasses such threshold. In this case, the antenna meets this requirement, not only with a single prototype but with multiple antenna units. With respect to the efficiency, the obtained value is also in the highest range, although direct comparisons in this case require caution, since the achievable efficiency depends not only on the feed but largely on the geometry of the radio telescope. Another aspect is the size of the feed, which in this case has been optimized for a compact form to minimize cryostat volume and facilitate cryogenic cooling.

IV. APPLICATION

Yebes Observatory is one of the technology development centers of the International VLBI Service for Geodesy and Astrometry (IVS) [31], and one of its main activities is the development of microwave receivers and antennas for

TABLE 2. Comparison of different QRFH feeds for radio astronomy.

Reference	Bandwidth	Size (L×W) *	Reflection	Efficiency **
[9]	2-12 GHz (6:1)	3.7λ × 4.0λ	< -10 dB	> 50% (a)
[11]	2-12 GHz (6:1)	4.3λ × 4.9λ	< -6 dB	> 47% (b)
[13]	4.6-24 GHz (5.2:1)	9.0λ × 9.6λ	< -8 dB	> 53% (c)
[14]	0.7-4.2 GHz (6:1)	5.0λ × 6.0λ	< -14 dB	> 57% (d)
[15]	1.5-15.5 GHz (10.3:1)	2.5λ × 8.3λ	< -7 dB	> 44% (e)
[16]	2.4-24 GHz (10:1)	7.4λ × 7.5λ	< -9 dB	> 55% (c)
This work	2.2-14 GHz (6.4:1)	4.4λ × 5.1λ	< -10 dB	> 55% (f)

*: Size in terms of wavelength (λ) at center frequency.

**: Predicted aperture efficiency on the indicated reflector topology (and its corresponding full subtended angle): (a) shaped dual reflector (100º), (b) offset Gregorian (98º), (c) offset Gregorian (116º), (d) prime focus (63º), (e) prime focus (159º), (f) displaced axis (130º).

the network. Recent works have been undertaken towards improving its overall radio-frequency front end design for VGOS, and the present QRFH feed solution provides superior performance compared to previous versions. After its successful validation, the five antenna units presented in this paper are going to be –or have already been– installed in their respective cryogenic receivers at different international stations of the VGOS network.

V. CONCLUSION

Extensive research has validated the effectiveness of QRFH antennas as wideband feeds for next-generation radio telescopes. Nevertheless, careful consideration must be given to the interaction between the waveguide modes within the horn to ensure proper performance of the feed over a wide bandwidth. This paper evidences the potential detrimental effects on the telescope efficiency caused by higher order modes excited from the single-ended transition of a QRFH feed. To address this problem, the proposed modular design approach allows both analyzing the distribution of modes at the throat of the QRFH antenna across the bandwidth and mitigating the non-fundamental modes with an appropriate design of the transition. Besides, this methodology simplifies the optimization process of the flared part and enables a seamless integration of the two antenna parts.

REFERENCES

[1] P. J. B. Clarricoats and A. D. Olver, *Corrugated Horns for Microwave Antennas*. U.K.: The Institution of Electrical Engineers, 1984.
[2] H. Schuh and D. Behrend, "VLBI: A fascinating technique for geodesy and astrometry," *J. Geodyn.*, vol. 61, pp. 68–80, Oct. 2012.
[3] P. E. Dewdney, P. J. Hall, R. T. Schilizzi, and T. J. L. W. Lazio, "The square kilometre array," *Proc. IEEE*, vol. 97, no. 8, pp. 1482–1496, Aug. 2009.
[4] J. Welch et al., "The Allen telescope array: The first widefield, panchromatic, snapshot radio camera for radio astronomy and SETI," *Proc. IEEE*, vol. 97, no. 8, pp. 1438–1447, Aug. 2009.
[5] G. Cortes-Medellin, "Non-planar quasi-self-complementary ultra-wideband feed antenna," *IEEE Trans. Antennas Propag.*, vol. 59, no. 6, pp. 1935–1944, Jun. 2011.

[6] J. Yang, M. Pantaleev, P.-S. Kildal, B. Klein, Y. Karandikar, L. Helldner, N. Wadefalk, and C. Beaudoin, "Cryogenic 2–13 GHz eleven feed for reflector antennas in future wideband radio telescopes," *IEEE Trans. Antennas Propag.*, vol. 59, no. 6, pp. 1918–1934, Jun. 2011.

[7] R. Gawande and R. Bradley, "Towards an ultra wideband low noise active sinuous feed for next generation radio telescopes," *IEEE Trans. Antennas Propag.*, vol. 59, no. 6, pp. 1945–1953, Jun. 2011.

[8] K. A. Abdalmalak, G. S. Botello, S. Llorente-Romano, A. Rivera-Lavado, J. Flygare, J. A. L. Fernándezs, J. M. S. Puente, L. E. García-Castillo, D. Segovia-Vargas, M. Pantaleev, and L. E. García-Muñoz, "Ultrawideband conical log-spiral circularly polarized feed for radio astronomy," *IEEE Trans. Antennas Propag.*, vol. 68, no. 3, pp. 1995–2007, Mar. 2020.

[9] A. Akgiray, S. Weinreb, W. A. Imbriale, and C. Beaudoin, "Circular quadruple-ridged flared horn achieving near-constant beamwidth over multioctave bandwidth: Design and measurements," *IEEE Trans. Antennas Propag.*, vol. 61, no. 3, pp. 1099–1108, Mar. 2013.

[10] O. B. Jacobs, J. W. Odendaal, and J. Joubert, "Quad-ridge horn antenna with elliptically shaped sidewalls," *IEEE Trans. Antennas Propag.*, vol. 61, no. 6, pp. 2948–2955, Jun. 2013.

[11] T. S. Beukman, P. Meyer, M. V. Ivashina, and R. Maaskant, "Modal-based design of a wideband quadruple-ridged flared horn antenna," *IEEE Trans. Antennas Propag.*, vol. 64, no. 5, pp. 1615–1626, May 2016.

[12] J. Shi, S. Weinreb, W. Zhong, X. Yin, and M. Yang, "Quadruple-ridged flared horn operating from 8 to 50 GHz," *IEEE Trans. Antennas Propag.*, vol. 65, no. 12, pp. 7322–7327, Dec. 2017.

[13] B. Dong, J. Yang, J. Dahlström, J. Flygare, M. Pantaleev, and B. Billade, "Optimization and realization of quadruple-ridge flared horn with new spline-defined profiles as a high-efficiency feed from 4.6 GHz to 24 GHz," *IEEE Trans. Antennas Propag.*, vol. 67, no. 1, pp. 585–590, Jan. 2019.

[14] K. W. Smart, A. Dunning, S. L. Smith, N. Carter, M. Bourne, P. Doherty, S. Castillo, and B. Dong, "Pattern measurements of cryogenically cooled ultra-wideband feed horn," in *Proc. 13th Eur. Conf. Antennas Propag. (EuCAP)*, Mar. 2019, pp. 1–4.

[15] J. Flygare and M. Pantaleev, "Dielectrically loaded quad-ridge flared horn for beamwidth control over decade bandwidth—Optimization, manufacture, and measurement," *IEEE Trans. Antennas Propag.*, vol. 68, no. 1, pp. 207–216, Jan. 2020.

[16] Y. Ma, C. H. See, F. Pang, D. Wu, D. Liu, Z. Z. Abidin, S. Keates, B. Peng, and R. A. Abd-Alhameed, "A 10:1 bandwidth cryogenic quadruple-ridged flared horn design for reflector antennas in radio astronomy," *IEEE Access*, vol. 8, pp. 81101–81115, 2020.

[17] J. Flygare, J. Yang, A. W. Pollak, R. E. J. Watkins, F. Hillier, L. Helldner, and S.-E. Ferm, "Beyond-decade ultrawideband quad-ridge flared horn with dielectric load from 1 to 20 GHz," *IEEE Trans. Antennas Propag.*, vol. 71, no. 3, pp. 2110–2125, Mar. 2023.

[18] T. S. Beukman, M. V. Ivashina, R. Maaskant, P. Meyer, and C. Bencivenni, "A quadraxial feed for ultra-wide bandwidth quadruple-ridged flared horn antennas," in *Proc. 8th Eur. Conf. Antennas Propag. (EuCAP)*, Apr. 2014, pp. 3312–3316.

[19] M. A. Morgan and S.-K. Pan, "Graphical prediction of trapped mode resonances in sub-mm and THz waveguide networks," *IEEE Trans. THz Sci. Technol.*, vol. 3, no. 1, pp. 72–80, Jan. 2013.

[20] R. Lehmensiek and D. I. L. de Villiers, "A method to design trapped-mode free quadruple-ridged flared horn antennas," in *Proc. 17th Eur. Conf. Antennas Propag. (EuCAP)*, Mar. 2023, pp. 1–4.

[21] W. Sun and C. A. Balanis, "Analysis and design of quadruple-ridged waveguides," *IEEE Trans. Microw. Theory Techn.*, vol. 42, no. 12, pp. 2201–2207, Dec. 1994.

[22] *CST Studio Suite*, Dassault Systèmes, Aix-en-Provence, France, 2018.

[23] W. Burnside and C. Chuang, "An aperture-matched horn design," *IEEE Trans. Antennas Propag.*, vol. AP-30, no. 4, pp. 790–796, Jul. 1982.

[24] P. Lavoie, "An introduction to NURBS," Ottawa Univ., Ottawa, ON, Canada, Tech. Rep., 1999.

[25] *Matlab*, MathWorks, Inc., MA, USA, 2018.

[26] A. P. Popov and T. Milligan, "Amplitude aperture-distribution control in displaced-axis two-reflector antennas," *IEEE Antennas Propag. Mag.*, vol. 39, no. 6, pp. 58–63, Dec. 1997.

[27] *GRASP*, version 9.2.01, TICRA, Copenhagen, Denmark.

[28] P.-S. Kildal, "Factorization of the feed efficiency of paraboloids and Cassegrain antennas," *IEEE Trans. Antennas Propag.*, vol. AP-33, no. 8, pp. 903–908, Aug. 1985.

[29] T. L. Wilson, K. Rohlfs, and S. Hüttemeister, *Tools of Radio Astronomy*, 6th ed. Berlin, Germany: Springer, 2013.

[30] A. Niell et al., "Demonstration of a broadband very long baseline interferometer system: A new instrument for high-precision space geodesy," *Radio Sci.*, vol. 53, no. 10, pp. 1269–1291, Oct. 2018.

[31] A. Nothnagel, T. Artz, D. Behrend, and Z. Malkin, "International VLBI service for geodesy and astrometry: Delivering high-quality products and embarking on observations of the next generation," *J. Geodesy*, vol. 91, no. 7, pp. 711–721, Jul. 2017.

ÓSCAR GARCÍA-PÉREZ was born in Madrid, Spain, in 1984. He received the M.Sc. and Ph.D. degrees in telecommunication engineering from Universidad Carlos III de Madrid, Spain, in 2007 and 2011, respectively. He is currently a RF Engineer with Yebes Observatory, Guadalajara, Spain. His main research interests include the design and development of microwave devices and antennas for radio astronomy, electromagnetic simulations, and radio frequency measurement techniques.

FÉLIX TERCERO was born in Madrid, Spain, in 1975. He received the M.S. degree in physics (electronic) from Universidad Complutense de Madrid in 1998. He is currently the Head of the Optics and Frontend Group, Yebes Observatory. The main projects in which he is involved are the development of instrumentation for the 40-m radio telescope and the 13.2-m RAEGE antennas. His main research interests include Gaussian beam optics, antenna simulation, beam wave guide systems, passive frontend components, microwave horns, and cryogenic receivers.

ALEJANDRO BALDOMINOS was born in Guadalajara, Spain, in 1995. He received the B.Eng. and M.Sc. degrees in telecommunications engineering from the University of Alcalá, Spain, in 2017 and 2019, respectively and the Ph.D. degree from Heriot-Watt University, U.K., in 2024. He is currently an RF Antenna Engineer with Airbus Defence and Space, U.K. His research interests include analysis and design of reflector antennas and signal processing for satellite communication systems.

GABRIEL GÓMEZ-MOLINA was born in Guadalajara, Spain, in 1990. He received the M.S. degree in telecommunication engineering from Universidad de Alcalá, Spain, in 2015. He is currently an RF Engineer with Yebes Observatory, Guadalajara, in the design of cryogenic receivers for radio astronomy. His main research interests include cryogenic systems, mechanics, and the integration of RF components into radio astronomy receivers.

ALBERTO GARCÍA-MERINO was born in Guadalajara, Spain, in 1997. He received the bachelor's and master's degrees in telecommunication engineering from the University of Alcalá, Spain, in 2019 and 2021, respectively. Since 2019, he has been with Yebes Observatory, first in the Frontend Design Team and more recently with the Cryogenic Low Noise Amplifier Development Team. His main research interest includes frontend components for radio astronomy receivers or other high sensitivity applications.

DAVID REGAJO-RODRÍGUEZ was born in Madrid, Spain, in 1983. He received the M.S. degree in telecommunication engineering from Universidad Carlos III de Madrid, Spain, in 2007. He is currently a FPGA Developer with Yebes Observatory, Guadalajara, Spain. His main research interests include the design and development of spectrometry techniques for radio astronomy, hardware-based UDP/IP communications, and radio frequency measurement techniques.

ROCÍO SÁNCHEZ-MONTERO (Member, IEEE) was born in Madrid, Spain, in 1979. She received the M.S. and Ph.D. degrees in telecommunications engineering from the University of Alcalá, Spain, in 2004 and 2011, respectively. She spent a half year with the Communications Group, The University of Sheffield, U.K., as a Predoctoral Research Fellow, in 2009, and a Postdoctoral Research Fellow, in 2017, for four months. She is currently an Associate Professor with the Department of Signal Processing and Communications, University of Alcalá, and a member of the Radiation and Sensing Research Group, University of Alcalá.